PAPER

Check for updates

Effects of size on the photocatalytic properties of high-index faceted pseudocubic and rhombohedral α-Fe₂O₃ nanocrystals†

Zhuan Wang,[a] Wenyu Xie,[b] Bo Yang,[a] Li Song,[a] Xueying Zhao,[a] Aslam Khan,[a] Fan Yue,[a] Xintai Su [ID][c] and Chao Yang [ID] *[a]

Size-controlled and high-index faceted α-Fe₂O₃ nanocrystals with pseudocubic and rhombohedral morphologies were synthesized through the hydrothermal treatment of β-FeOOH at different pHs. The size effect on the photocatalytic oxygen evolution efficiency of high-index faceted α-Fe₂O₃ nanocrystals was investigated. Rhombohedral α-Fe₂O₃ (pH 6.0) exhibits an outstanding apparent quantum yield of 9.93% and an oxygen evolution efficiency of 20.3%, which can be attributed to the optimal size and high-indexed {104} planes. This work provides a new idea for the design of high activity water oxidation catalysts, through the size optimization of high-index faceted materials.

Introduction

Given the growing energy consumption and environmental pollution caused by fossil fuel combustion, one of the biggest challenges of this century is the search for clean and renewable energy sources.[1] Currently, the direct conversion of solar energy into chemical energy by photocatalytic water splitting has aroused widespread interest. Nonetheless, in the water splitting context, the water oxidation reaction has to overcome higher energy barriers, and is thought to be the bottleneck of water splitting.[2] Thus, much effort has been devoted to the design and construction of highly efficient water oxidation catalysts (WOCs). Although IrO₂ and RuO₂ are considered to be the most efficient catalysts for water oxidation,[3,4] their extremely high cost makes researchers turn their research enthusiasm to cheap transition metal catalysts. A large number of transition metal compounds, including Co,[5,6] Cu,[7] Mn,[8–10] W,[11–13] and Fe,[14–16] have been explored as WOCs. Among these compounds, iron-based WOCs have attracted much attention due to their low cost and low toxicity.[17,18]

α-Fe₂O₃, because of its proper bandgap, has been extensively utilized as the photocatalyst or cocatalyst for oxygen evolution,[19]

[a]Ministry Key Laboratory of Oil and Gas Fine Chemicals, College of the Chemistry and Chemical Engineering, Xinjiang University, Urumqi 830046, China. E-mail: jerryyang1924@163.com

[b]Guangdong Provincial Key Laboratory of Petrochemcial Pollution Processes and Control, School of Environmental Science and Engineering, Guangdong University of Petrochemical Technology, Maoming, Guangdong 525000, China

[c]The Key Laboratory of Pollution Control and Ecosystem Restoration in Industry Clusters (Ministry of Education), School of Environment and Energy, South China University of Technology, Guangzhou 510006, China

† Electronic supplementary information (ESI) available. See DOI: 10.1039/c9ra08561k

hydrogen evolution,[20] CO₂ reduction,[21] and pollutant degradation.[22–24] Considerable effort has been devoted to improving the photocatalytic oxygen evolution of α-Fe₂O₃ based on the heterojunction construction.[25–30] The composite structure of α-Fe₂O₃/rGO significantly improves the charge carries separation of α-Fe₂O₃ and enhances the photocatalytic water oxidation performance.[28] The tight hetero-junction structure of α-Fe₂O₃/g-C₃N₄ has been demonstrated as active sites for visible-light-driven oxygen generation.[25] The optimized integration of cocatalyst CoOₓ enables hexagonal α-Fe₂O₃ nanoplates with dramatically enhanced O₂ evolution rate.[26] The Pt nanoparticles decorated α-Fe₂O₃ nanoplates structure exhibit the enhanced photoactivity and photostability for water oxidation.[27] Besides, the fabrication of α-Fe₂O₃ nanocrystals with specific shapes and sizes is also conducive to enhance the photocatalytic oxygen evolution ability. Moreover, the shape effect is essentially due to the arrangement of atoms on different exposed crystal faces. Plenty of work has confirmed that the {012} and {104} planes of α-Fe₂O₃ are high-index planes.[31–34] Ma *et al.* found that the exposed {104} planes of α-Fe₂O₃ exhibits excellent gas sensing properties.[33] Zhao *et al.* investigated that α-Fe₂O₃ nanocubes exposed {012} active facets combination with graphene lead to boosted lithium storage capability.[34] Recently, Xiang and co-workers reported that α-Fe₂O₃ nanocubes with {012} facets have much higher photocatalytic water oxidation activity than α-Fe₂O₃ nanoflakes with {001} facets.[31] Wang *et al.* researched that α-Fe₂O₃ enclosed by {012} and {104} facets can facilitate to increase the activity of photocatalytic oxygen evolution significantly.[32] However, the size effect on the photocatalytic water oxidation performance of α-Fe₂O₃ nanocrystals has been scarcely investigated. Moreover, the attempt to combine the size effect with the high-index facet to improve the photocatalytic activity of α-Fe₂O₃ is significant.

Here, we selectively synthesized pseudocubic and rhombohedral α-Fe$_2$O$_3$ nanocrystals with varying sizes through the hydrothermal treatment of the β-FeOOH precursor at different pH values. By adjusting the pH value of the precursor, a morphology evolution of α-Fe$_2$O$_3$ nanocrystals from {012} pseudocubes to {104} rhombohedrons was observed with the reduction in size. Through a comprehensive investigation of the factors affecting the oxygen production performance of the catalyst, we confirm the size-dependent photocatalytic water oxidation property of α-Fe$_2$O$_3$. Moreover, we obtained {104} planes faceted Fe$_2$O$_3$ (pH 6.0) possessing excellent photocatalytic oxygen evolution performance.

Experimental

Materials

Ferric chloride hexahydrate (FeCl$_3$·6H$_2$O), sodium hydroxide (NaOH) were purchased from Tianjin Zhiyuan Chemical Reagent Co., Ltd. All chemicals were of analytical grade and used directly without further purification.

Fabrication of α-Fe$_2$O$_3$ nanocrystals

The synthesis route was carried out according to the literature with a slight modification.[35] When synthesizing α-Fe$_2$O$_3$, 0.024 mol FeCl$_3$·6H$_2$O was dissolved in 600 mL deionized water, refluxed and stirred at 78 °C for 12 h to obtain a brown β-FeOOH solution with an initial pH value of 1.2 (measured by a LICHEN pH meter). The solution was divided into four equal portions, and the pH value of each portion was tuned with NaOH (1 mol L^{-1}) aqueous solution to 1.2, 2.0, 4.0, and 6.0, respectively. Subsequently, four 1 L Teflon autoclaves were used to encapsulate the β-FeOOH solutions with different pHs, which were then heated to 150 °C for 10 h. After natural cooling to room temperature, it was washed with ethanol and water several times and dried at 40 °C. The final products were labeled as Fe$_2$O$_3$-1.2, Fe$_2$O$_3$-2.0, Fe$_2$O$_3$-4.0, and Fe$_2$O$_3$-6.0, respectively.

Characterizations

The crystalline phase of the as-synthesized products was identified by X-ray diffraction (XRD) (BRUKER D8 Advance) at a scanning rate of 5° min^{-1} in 2θ ranging from 10° to 80°. A Hitachi S-4800 scanning electron microscope was used to obtain the scanning electron microscopy (SEM) images at 5 kV. The transmission electron microscopy (TEM) images were obtained on an FEI Tecnai G2 f20 s-twin with an accelerating voltage of 200 kV. The UV-vis absorption spectra of as-obtained catalysts were obtained by a Hitachi U-3010 spectrophotometer. The Brunauer–Emmett–Teller (BET) surface areas of the products were evaluated by N$_2$ adsorption–desorption measurements at 77 K (liquid nitrogen) in an automated surface area and porosity analyzer (ASAP2020, Micromeritics, USA). Photoluminescence spectra (PL) of the catalysts were characterized with a fluorescence spectrophotometer (Hitachi-F-4500) with an exciting wavelength of 300 nm. The particle size distribution was measured by Nanomeasure software.

Photocatalytic oxygen evolution measurements

Photocatalytic water oxidation tests were performed in a buffer solution with an argon atmosphere at room temperature. In this experiment, 5.0 mg of α-Fe$_2$O$_3$ was dispersed in a 10.0 mL 80.0 mM sodium borate buffer solution containing 1.0 mM [Ru(bpy)$_3$](ClO$_4$)$_2$ and 20.0 mM Na$_2$S$_2$O$_8$, and sealed with a rubber gasket in a 20 mL round-bottom flask. The solution was to degas the air with argon and then irradiated it with visible light (300 W Xe lamp, $\lambda > 420$ nm) at room temperature. Every two minutes, O$_2$ in the top air was sampled with a 100 μL syringe and analyzed by GC-TCD equipped with a 5 Å molecular sieve column.

Photoelectrochemical measurements

The transient photocurrent response was performed on a Chi 660D electrochemical workstation using a standard three-electrode system with Ag/AgCl and Pt electrodes as the counter and reference electrodes, respectively. The working electrode was prepared as follows: 5.0 mg of the as-synthesized sample was mixed with 1.0 mL of deionized water by ultrasonic treatment. Then, the mixture was coated on a 2.5 cm × 1.5 cm F-doped SnO$_2$-coated glass (FTO glass) electrode with approximately uniform thickness. Subsequently, the electrode was dried in vacuum at 110 °C for 10 h, and 0.5 mM Na$_2$S$_2$O$_4$ aqueous solution was used as the electrolyte.

Results and discussion

Fig. 1 exhibits the XRD patterns of the precursor and products. All products have obvious diffraction peaks at $2\theta = 24.26°$, 33.22°, 35.73°, 40.95°, 43.65°, 49.54°, 54.10°, 57.61°, 62.50°, and 64.07° could be indexed to the (012), (104), (110), (113), (024), (116), (018), (214), and (300) crystal planes, corresponding to the hexagonal hematite (JCPDS no. 33-0664). This result indicates that precursor β-FeOOH (JCPDS no. 34-1266) was completely transformed into to α-Fe$_2$O$_3$ through the hydrothermal treatment under different initial pHs.[36] The average crystallite sizes of α-Fe$_2$O$_3$ nanocrystals prepared at pH values of 1.2, 2.0, 4.0, and 6.0 were 50.61, 42.92, 39.99, and 37.06 nm, respectively, which were calculated by Scherrer formula.[37] The result demonstrates the crystallite size of the sample decrease with the increasing of precursor pH value.
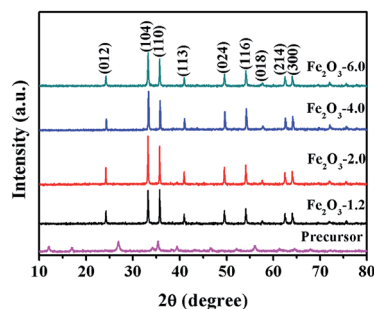

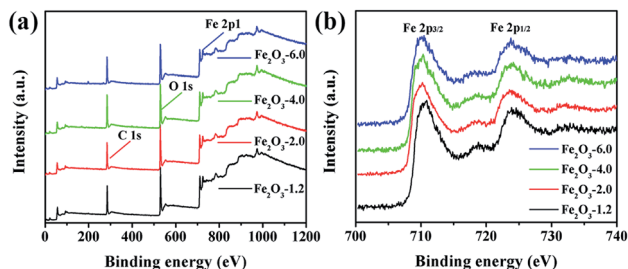**Fig. 1** XRD patterns of the precursor and samples Fe$_2$O$_3$-x (x is 1.2, 2.0, 4.0, and 6.0).

Fig. 2 XPS spectra of α-Fe$_2$O$_3$ nanocrystals: (a) full survey spectrum of Fe$_2$O$_3$-x (x is 1.2, 2.0, 4.0, and 6.0); (b) Fe 2p peaks of Fe$_2$O$_3$-x.

For further identifying the samples, the surface composition of the products was analyzed by XPS in Fig. 2. The XPS spectra of the samples display the same line shape, and the presence of Fe, O, and C elements in Fig. 2a demonstrates that the four substances have the same valence state of elements. The binding energy peaks at 710.3 and 723.8 eV in the Fe 2p high-resolution XPS spectrum (Fig. 2b) are attributed to Fe 2p$_{3/2}$ and Fe 2p$_{1/2}$, respectively, which strongly proves that Fe element in iron oxide exists in the form of the Fe^{3+}. The lineshape and binding energies of Fe 2p agree well with those reported in the literature.[38]

The size and morphology of the α-Fe$_2$O$_3$ nanocrystals were characterized by SEM in Fig. 3. The schematic illustration in Fig. 3a shows the morphology and size evolution of α-Fe$_2$O$_3$ nanocrystals with varying pH values. Fig. 3b and c exhibit the products of Fe$_2$O$_3$-1.2 and Fe$_2$O$_3$-2.0 have the same pseudocubic morphology and different mean lengths of ca. 603 and 507 nm,

respectively. Moreover, rhombohedral α-Fe$_2$O$_3$ with different average sizes of ca. 145 and 88 nm were obtained at pH 4.0 and 6.0, respectively (Fig. 3d and e). It is worth mentioning that the rough surface of pseudocubes mirrors the growth nature of the iron oxide, which is formed by the aggregation and fusion of plenty of small particles. The crystal growth behavior at the expense of small particles is consistent with the description of the Ostwald ripening mechanism.[39] Hence, the Ostwald ripening mechanism could be used to explain α-Fe$_2$O$_3$ growth behavior. Overall, the pH control process discloses that increasing the precursor pH not only contributes to the formation of smaller α-Fe$_2$O$_3$ nanocrystals but also driving the shape transformation of α-Fe$_2$O$_3$ from pseudocubic to rhombohedron.
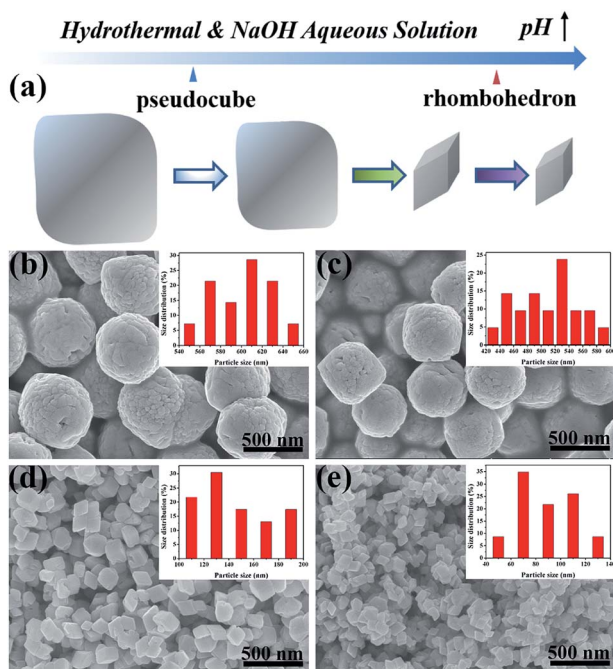

Fig. 3 (a) Schematic illustration of the growth of α-Fe$_2$O$_3$ with pH change; (b–e) SEM images of the samples and inset of corresponding particle size distribution, (b) Fe$_2$O$_3$-1.2, (c) Fe$_2$O$_3$-2.0, (d) Fe$_2$O$_3$-4.0, and (e) Fe$_2$O$_3$-6.0.
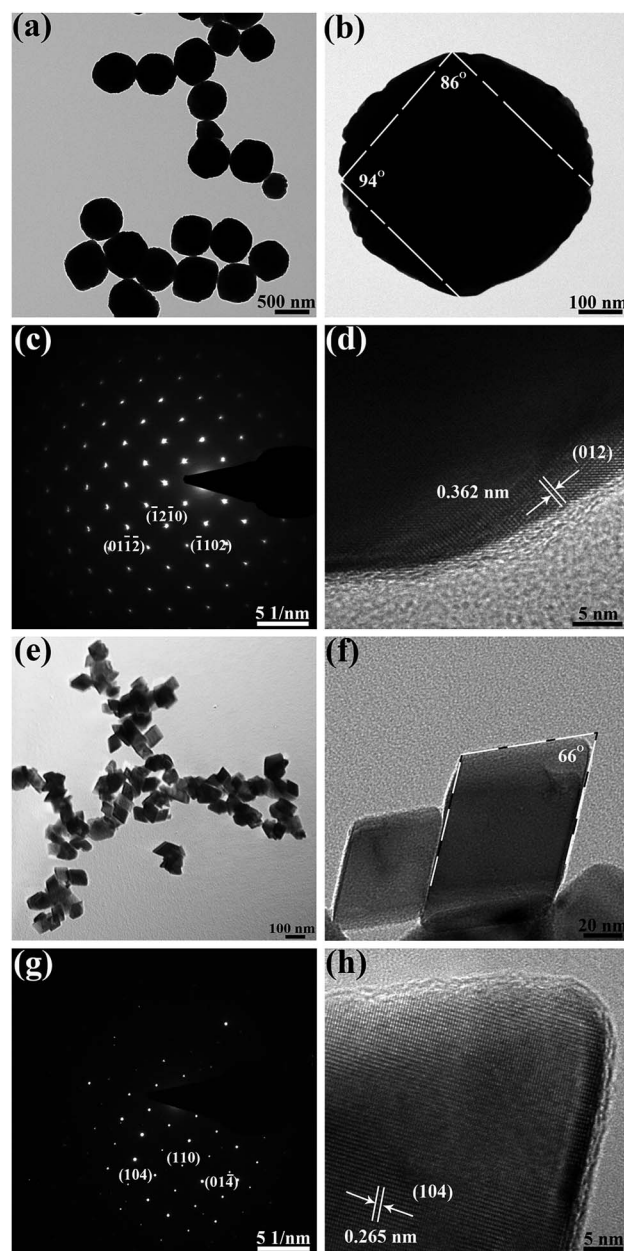

Fig. 4 (a, b) and (e, f) TEM, (c) and (g) SAED, (d) and (h) HRTEM images of pseudocubic α-Fe$_2$O$_3$ (pH 1.2) and rhombohedral α-Fe$_2$O$_3$ (pH 6.0), respectively.
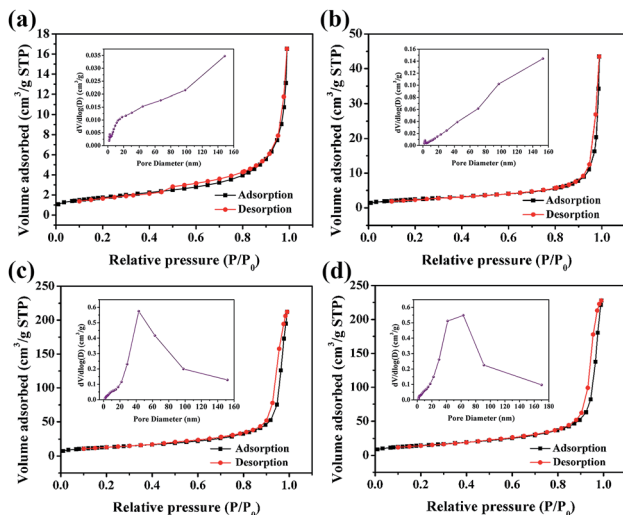
Fig. 5 N$_2$ adsorption–desorption isotherm of sample (inset of Barrett–Joyner–Halenda pore size), (a) Fe$_2$O$_3$-1.2, (b) Fe$_2$O$_3$-2.0, (c) Fe$_2$O$_3$-4.0, and (d) Fe$_2$O$_3$-6.0.

High-resolution transmission electron microscopy (HRTEM) was employed to recognize the dominant active crystal planes of the two typical samples Fe$_2$O$_3$-1.2 and Fe$_2$O$_3$-6.0. TEM images and selected area electron diffraction (SAED) pattern of the pseudocubic α-Fe$_2$O$_3$ (pH 1.2) are exhibited in Fig. 4a–d. Pseudocubic exhibits rhombus facets with dihedral angles between two adjacent facets are 86° and 94° (Fig. 4b). The ordered diffraction spots in the SEAD pattern (Fig. 4c) present the single-crystalline structure of the pseudocubes. Further, the HRTEM shows the measured lattice spacing of the exposed facet is 0.362 nm (Fig. 4d), corresponding to the (012) facet of α-Fe$_2$O$_3$. The above characteristics are consistent with the single-crystal α-Fe$_2$O$_3$ pseudocubes enclosed by {012} planes reported in the literature.[40,41] Fig. 4e–g exhibits the TEM images and SAED pattern of the rhombohedral α-Fe$_2$O$_3$ (pH 6.0). TEM images in Fig. 4e and g reveal that the nanocrystals are α-Fe$_2$O$_3$ rhombohedrons with a single-crystalline structure. The measured lattice fringe (Fig. 4h) is of 0.265 nm, agree well with (104) plane of α-Fe$_2$O$_3$. The dihedral angle measured in Fig. 4f is 66°, which can match with the theoretical value of 64.9°.[42] These descriptions of α-Fe$_2$O$_3$ (pH 6.0) are in agreement with the characteristics of rhombohedral iron oxide enclosed by {104} planes.[43]

Brunauer–Emmett–Teller (BET) adsorption/desorption isotherms and Barrett–Joyner–Halenda (BJH) pore size were used to characterize the surface properties of the catalysts
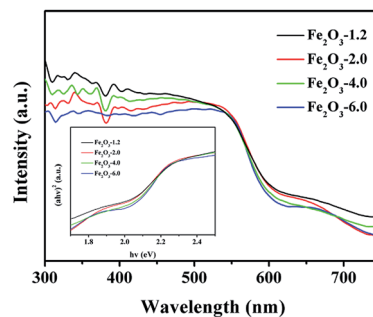

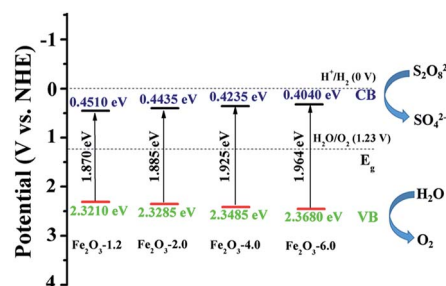Fig. 6 UV-visible diffuse reflectance spectra of Fe$_2$O$_3$-x (inset of Tauc plots).

Fig. 7 Schematic drawing of redox potentials of Fe$_2$O$_3$-x.

(Fig. 5). Each isotherm corresponds to a type IV isotherm with a small hysteresis loop, indicating the presence of mesopores in the catalyst. The pore size distribution curves of four α-Fe$_2$O$_3$ samples show that the pore size distribution ranges from 1.7 to 170 nm, which confirms the existence of mesopores and macropores. The specific surface areas (Table 1) of catalysts calculated by the BET method are 6.29, 8.93, 47.03, and 52.70 m^2 g^{-1} corresponding to Fe$_2$O$_3$-1.2, Fe$_2$O$_3$-2.0, Fe$_2$O$_3$-4.0, and Fe$_2$O$_3$-6.0, respectively.

UV-vis diffuse reflectance spectra (Fig. 6) show that the absorption edges of all samples are longer than 600 nm, which reflects the strong visible-light-harvesting ability of samples. Moreover, the absorption band edge of the product is blue-shifted with an increase of the pH value, which could result from the quantum size effect.[44] The bandgap of samples was determined from the Tauc plot (inset of Fig. 6), claiming the indirect bandgap of samples is 1.870, 1.885, 1.925, and 1.964 eV, respectively. Combined with Mulliken electronegativity theory ($E_{CB} = X - E_C - 1/2E_g$, $E_{VB} = E_{CB} + E_g$, where X is absolute electronegativity, E_C is the energy of free electrons, E_{VB} is the

Table 1 Physicochemical properties and oxygen evolution activities of α-Fe$_2$O$_3$ samples

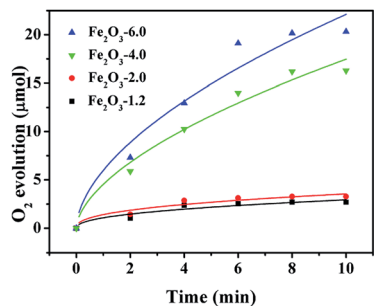| Catalysts	Morphology	Dominant facets	Specific surface area (m^2 g^{-1})	O$_2$ evolution (μmol)
Fe$_2$O$_3$-1.2	Pseudocubic	{012}	6.29	2.71
Fe$_2$O$_3$-2.0	Pseudocubic	—	8.93	3.28
Fe$_2$O$_3$-4.0	Rhombohedron	—	47.03	16.28
Fe$_2$O$_3$-6.0	Rhombohedron	{104}	52.70	20.32

Fig. 8 Plots of oxygen evolution *vs.* time for visible-light-driven water oxidation by α-Fe₂O₃ nanocrystals. Condition: 5.0 mg catalyst, Xe lamp, 300 W, $\lambda > 420$ nm, 100 mW cm^{-2}, 10 min lumination, 1.0 mM [Ru(bpy)₃](ClO₄)₂, 20.0 mM Na₂S₂O₈, 80.0 mM sodium borate buffer (initial pH 9.0).

potential of the conduction band, and E_{VB} is the potential of the valence band),[45] the E_{VB} and E_{CB} of the four samples are determined. As seen in Fig. 7, the valence bands of the semiconductors are greater than 1.23 V, which meets the requirement of oxygen evolution kinetics. Moreover, the valence band becomes more positive with the increase of pH value, implying the enhance of water oxidation ability.

The curves in Fig. 8 display the amount of oxygen evolution of the four α-Fe₂O₃ samples follows the order of Fe₂O₃-6.0 > Fe₂O₃-4.0 > Fe₂O₃-2.0 > Fe₂O₃-1.2. In particular, Fe₂O₃-6.0 possesses the maximum oxygen evolution of 20.32 μmol, almost 7.5 times that of Fe₂O₃-1.2 (2.71 μmol). In order to comprehensively analyze the influence of size and crystal surface factors on the oxygen production performance of the catalysts, we calculated the specific activity of the four samples. It can be seen intuitively that the specific activity of the four samples has not much difference (Fig. 9), especially the difference between Fe₂O₃-6.0 and Fe₂O₃-1.2 can almost be seen as a deviation. This result reflects size effect is the primary factor, which determines the oxygen evolution efficiency of {104} planes faceted Fe₂O₃-6.0 superior to that of other catalysts. Moreover, compared with other iron-based catalysts (Table 2), Fe₂O₃-6.0 has an outstanding apparent quantum yield of 9.93% and an oxygen evolution efficiency of 20.3%, which could be ascribed to the optimal size and high-activity planes. After five times of oxygen evolution performance test (Fig. 10), the oxygen evolution did
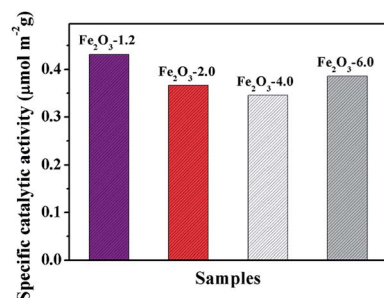
Table 2 Comparison of catalytic performance of different catalysts

Catalysts	O₂ (μmol)	O₂ yield[a] (%)	Reference
Fe₂C	10.32	20.64	49
Fe₂O₃	2.83	17.7	31
Fe₂O₃-6.0	20.32	20.32	This work
Fe₂O₃-4.0	16.28	16.28	This work
Fe₂O₃-2.0	3.28	3.28	This work
Fe₂O₃-1.2	2.71	2.71	This work
FeOOH	7.91	3.955	50
NiFe₂O₄	3.7	7.40	51

[a] Yield is defined as twice the number of moles of O₂ per mole of Na₂S₂O₈.

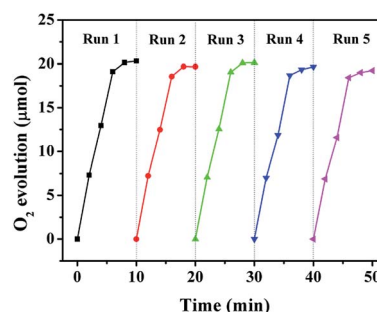**Fig. 10** Photostability study of Fe₂O₃-6.0 in the water oxidation reaction. Condition: 5.0 mg catalyst, Xe lamp, 300 W, $\lambda > 420$ nm, 100 mW cm^{-2}, 1.0 mM [Ru(bpy)₃](ClO₄)₂, 20.0 mM Na₂S₂O₈, 80.0 mM sodium borate buffer (initial pH 9.0).

not decrease obviously, indicating Fe₂O₃-6.0 has excellent cycle stability. We further analyzed the valence states and surface properties of the sample Fe₂O₃-6.0 before and after the photocatalytic reaction by XPS. Fig. 11a and (b) show the high-resolution XPS spectra of Fe 2p and O 1s before and after the reaction. The binding energy of each element has not changed. Therefore, we conclude that the superior performance stability can be ascribed to the stable structure.

The charge transfer kinetics was studied utilizing photocurrent response and electrochemical impedance spectroscopy (EIS). The photocurrent response curves (Fig. 12a) show an intensity order: Fe₂O₃-6.0 > Fe₂O₃-4.0 > Fe₂O₃-2.0 > Fe₂O₃-1.2, demonstrating Fe₂O₃-6.0 with optimal charge separation efficiency. EIS plot (Fig. 12b) discloses Fe₂O₃-6.0 has the fastest

Fig. 9 Specific catalytic activities (the amount of O₂ per unit surface area) of α-Fe₂O₃ samples.

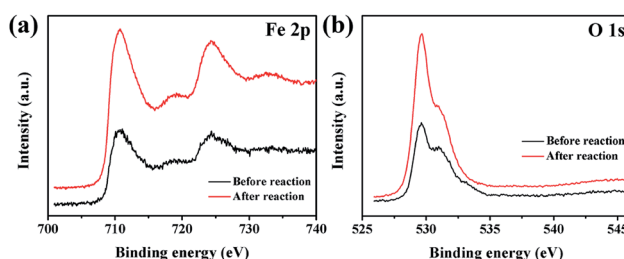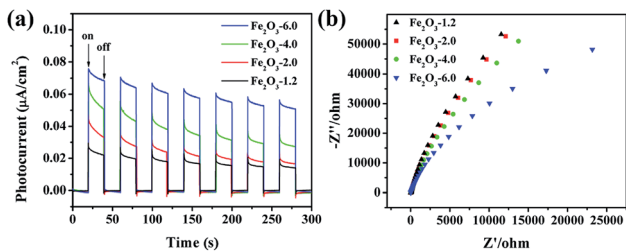**Fig. 11** XPS spectra of Fe₂O₃-6.0 before and after photocatalytic reaction, Fe 2p (a) and O 1s (b).

Fig. 12 (a) Photocurrent response diagrams of the Fe_2O_3-x under visible irradiation; (b) EIS Nyquist plots of the Fe_2O_3-x.
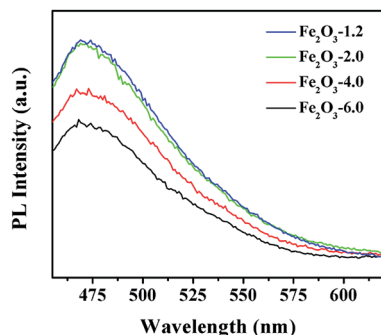

Fig. 13 PL spectra of the as-prepared Fe_2O_3 samples.

electron transport according to the smallest semicircular, corresponding to the photocurrent result. For further investigating the separation and recombination of electron–hole pairs, the photoluminescence (PL) spectra of the catalysts were recorded at room temperature. As shown in Fig. 13, α-Fe_2O_3 has a strong peak near 470 nm which attributed to the excitonic PL spectrum.[46] The dramatically decreased PL intensity of the α-Fe_2O_3 samples reflects the higher separation efficiency of photoinduced electron–hole pairs and higher photocatalytic activity,[47] which can be ascribed to the shorten transportation path of photogenerated electrons and holes resulting from the reduction of catalyst size.[48]

Conclusions

In summary, we prepared high-index faceted α-Fe_2O_3 with different sizes in a facile way. We demonstrated that the photocatalytic oxygen evolution efficiency of α-Fe_2O_3 nanocrystals is strongly dependent on the size. Moreover, the optimal size and high-indexed {104} planes endow rhombohedral α-Fe_2O_3 with excellent water oxidation performance. This study offers a feasible way for the construction of highly efficient water oxidation catalysts through the size tuning of high-index faceted materials.

Conflicts of interest

There are no conflicts of interest to declare.

Acknowledgements

References

1 J. Li, R. Guttinger, R. More, F. Song, W. Wan and G. R. Patzke, *Chem. Soc. Rev.*, 2017, **46**, 6124–6147.

2 G. Chen, L. Chen, S. M. Ng and T. C. J. C. Lau, *ChemSusChem*, 2014, **7**, 127–134.

3 F. A. Frame, T. K. Townsend, R. L. Chamousis, E. M. Sabio, T. Dittrich, N. D. Browning and F. E. Osterloh, *J. Am. Chem. Soc.*, 2011, **133**, 7264–7267.

4 J. Sato, N. Saito, Y. Yamada, K. Maeda, T. Takata, J. N. Kondo, M. Hara, H. Kobayashi, K. Domen and Y. Inoue, *J. Am. Chem. Soc.*, 2005, **127**, 4150–4151.

5 Z. Wan, Q. Xu, H. Li, Y. Zhang, Y. Ding and J. Wang, *Appl. Catal., B*, 2017, **210**, 67–76.

6 Q. Xu, H. Li, L. Chi, L. Zhang, Z. Wan, Y. Ding and J. Wang, *Appl. Catal., B*, 2017, **202**, 397–403.

7 S. M. Barnett, K. I. Goldberg and J. M. Mayer, *Nat. Chem.*, 2012, **4**, 498.

8 G. C. Dismukes, R. Brimblecombe, G. A. Felton, R. S. Pryadun, J. E. Sheats, L. Spiccia and G. F. Swiegers, *Acc. Chem. Res.*, 2009, **42**, 1935–1943.

9 R. Brimblecombe, A. Koo, G. C. Dismukes, G. F. Swiegers and L. Spiccia, *J. Am. Chem. Soc.*, 2010, **132**, 2892–2894.

10 S. Sun, G. Shen, J. Jiang, W. Mi, X. Liu, L. Pan, X. Zhang and J.-J. Zou, *Adv. Energy Mater.*, 2019, **9**, 1901505.

11 F. Amano, E. Ishinaga and A. Yamakata, *J. Phys. Chem. C*, 2013, **117**, 22584–22590.

12 G. R. Bamwenda, T. Uesigi, Y. Abe, K. Sayama and H. Arakawa, *Appl. Catal., A*, 2001, **205**, 117–128.

13 J. Huang, Y. Zhang and Y. Ding, *ACS Catal.*, 2017, 7, 1841–1845.

14 S. J. Kim, Y. Lee, D. K. Lee, J. W. Lee and J. K. Kang, *J. Mater. Chem. A*, 2014, **2**, 4136–4139.

15 J. Zhu, Z. Yin, D. Yang, T. Sun, H. Yu, H. E. Hoster, H. H. Hng, H. Zhang and Q. Yan, *Energy Environ. Sci.*, 2013, **6**, 987–993.

16 Y.-C. Zhang, N. Afzal, L. Pan, X. Zhang and J.-J. Zou, *Adv. Sci.*, 2019, **6**, 1900053.

17 W. C. Ellis, N. D. McDaniel, S. Bernhard and T. J. Collins, *J. Am. Chem. Soc.*, 2010, **132**, 10990–10991.

18 T. K. Townsend, E. M. Sabio, N. D. Browning and F. E. Osterloh, *Energy Environ. Sci.*, 2011, **4**, 4270–4275.

19 J. Zhu, Z. Yin, D. Yang, T. Sun, H. Yu, H. E. Hoster, H. H. Hng, H. Zhang and Q. Yan, *Energy Environ. Sci.*, 2013, **6**, 987–993.

20 Z. Lin, C. Du, B. Yan and G. Yang, *Catal. Sci. Technol.*, 2019, **9**, 5582–5592.

21 Z. Guo, G. Chen, C. Cometto, B. Ma, H. Zhao, T. Groizard, L. Chen, H. Fan, W.-L. Man and S.-M. J. N. C. Yiu, *Nat. Catal.*, 2019, **2**, 801–808.

22 A. Kusior, K. Michalec, P. Jelen and M. Radecka, *Appl. Surf. Sci.*, 2019, **476**, 342–352.

23 M. R. Abhilash, A. Gangadhar, J. Krishnegowda, M. Chikkamadaiah and S. Srikantaswamy, *RSC Adv.*, 2019, **9**, 25158–25169.

24 G. Shen, L. Pan, Z. Lü, C. Wang, F.-e. Aleem, X. Zhang and J.-J. Zou, *Chin. J. Catal.*, 2018, **39**, 920–928.

25 X. She, J. Wu, H. Xu, J. Zhong, Y. Wang, Y. Song, K. Nie, Y. Liu, Y. Yang and M. T. F. Rodrigues, *Adv. Energy Mater.*, 2017, **7**, 1700025.

26 L. Li, X. She, J. Yi, L. Pan, K. Xia, W. Wei, X. Zhu, Z. Chen, H. Xu and H. Li, *Appl. Surf. Sci.*, 2019, **469**, 933–940.

27 H. Liu, K. Tian, J. Ning, Y. Zhong, Z. Zhang and Y. Hu, *ACS Catal.*, 2019, **9**, 1211–1219.

28 F. Meng, J. Li, S. K. Cushing, J. Bright, M. Zhi, J. D. Rowley, Z. Hong, A. Manivannan, A. D. Bristow and N. Wu, *ACS Catal.*, 2013, **3**, 746–751.

29 X.-T. Xu, L. Pan, X. Zhang, L. Wang and J.-J. Zou, *Adv. Sci.*, 2019, **6**, 1801505.

30 Z.-S. Pourbakhsh, K. Mohammadi, A. Moshaii, M. Azimzadehirani and A. Hosseinmardi, *RSC Adv.*, 2019, **9**, 31860–31866.

31 Q. Xiang, G. Chen and T.-C. Lau, *RSC Adv.*, 2015, **5**, 52210–52216.

32 Y. L. Wang, Y. H. Li, X. L. Wang, Y. Hou, A. P. Chen and H. G. Yang, *Appl. Catal., B*, 2017, **206**, 216–220.

33 Y. Ma, J. Yang, Y. Yuan, H. Zhao, Q. Shi, F. Zhang, C. Pei, B. Liu and H. Yang, *Langmuir*, 2017, **33**, 8671–8678.

34 Y. Zhao, D. Yan, C. Ding, D. Su, Y. Ge, Y. Zhao, H. Zhou, J. Li and H. Jin, *J. Power Sources*, 2016, **327**, 658–665.

35 X. Rao, X. Su, C. Yang, J. Wang, X. Zhen and D. Ling, *CrystEngComm*, 2013, **15**, 7250–7256.

36 G. Zhang, Y. Shi, H. Wang, L. Jiang, X. Yu, S. Jing, S. Xing and P. Tsiakaras, *J. Power Sources*, 2019, **416**, 118–124.

37 A. Patterson, *Phys. Rev.*, 1939, **56**, 978.

38 J. S. Hu, L. S. Zhong, W. G. Song and L. J. Wan, *Adv. Mater.*, 2008, **20**, 2977–2982.

39 W. Yang, F. Gao, G. Wei and L. An, *Cryst. Growth Des.*, 2009, **10**, 29–31.

40 K. He, B. Song, L. Zhan, W. Lu, J. Li, G. Zhao and G. Han, *CrystEngComm*, 2016, **18**, 754–758.

41 J. Cai, S. Chen, J. Hu, Z. Wang, Y. Ma and L. Qi, *CrystEngComm*, 2013, **15**, 6284–6288.

42 R. D. Rodriguez, D. Demaille, E. Lacaze, J. Jupille, C. Chaneac and J.-P. Jolivet, *J. Phys. Chem. C*, 2007, **111**, 16866–16870.

43 M. Lin, H. R. Tan, J. P. Y. Tan and S. Bai, *J. Phys. Chem. C*, 2013, **117**, 11242–11250.

44 A. I. Ekimov, A. L. Efros and A. A. Onushchenko, *Solid State Commun.*, 1985, **56**, 921–924.

45 J. P. Perdew, R. G. Parr, M. Levy and J. L. Balduz Jr, *Phys. Rev. Lett.*, 1982, **49**, 1691.

46 L. Yu, Y. Zhang, J. He, H. Zhu, X. Zhou, M. Li, Q. Yang and F. Xu, *J. Alloys Compd.*, 2018, **753**, 601–606.

47 X. An, D. Cheng, L. Dai, B. Wang, H. J. Ocampo, J. Nasrallah, X. Jia, J. Zou, Y. Long and Y. Ni, *Appl. Catal., B*, 2017, **206**, 53–64.

48 F. E. Osterloh, *Chem. Soc. Rev.*, 2013, **42**, 2294–2320.

49 M. Zhang, J. Luo, X. Liang, B. Yan, M. Baikenov, X. Su, L. Chi and C. Yang, *Mater. Lett.*, 2018, **210**, 73–76.

50 L. Chi, Q. Xu, X. Liang, J. Wang and X. Su, *Small*, 2016, **12**, 1351–1358.

51 D. Hong, Y. Yamada, T. Nagatomi, Y. Takai and S. Fukuzumi, *J. Am. Chem. Soc.*, 2012, **134**, 19572–19575.